Characterization of Bi-incorporated InSb(111)A/B Surfaces

An STM and XPS Study

Shengpeng Huang

Synchrotron Radiation Research Division

Department of Physics, Faculty of Science

Degree: Master of Science

Duration: 12 months

LUND UNIVERSITY

Supervisor and Co-Supervisor:
Rainer Timm
Rohit Yadav

6th October 2023

Abstract

In recent years, III-V semiconductor materials have received increasing attention due to their admirable electronic properties like direct tunable bandgaps and high charge carrier mobility. Indium Antimonide (InSb) possesses the largest electron mobility among III-V materials and is promising for infrared detectors, high-speed field effect transistors, and spintronics. Incorporation of bismuth (Bi) into III-V semiconductors can enhance spin-orbit coupling and reduce the band gap. To modify III-V semiconductors with the desired electronic properties and eventually allow industrial fabrication, there are a few challenges to overcome. One is to understand surface modifications.

In this study, the surface properties of InSb(111)A/B with Bi incorporation are investigated with highly surface-sensitive characterization techniques of scanning tunneling microscopy (STM) and X-ray photoelectron spectroscopy (XPS). Clean InSb(111)A and InSb(111)B surfaces exhibit (2×2) and (3×3) reconstructions, respectively. After the Bi deposition, the surfaces display amorphous Bi aggregations. An Sb-Bi bonding configuration is found on the Bi-deposited surface, followed by a Bi-Bi component corresponding to a metallic Bi layer. The Bi spectra of a sequence of deposition and annealing steps are discussed.

Acknowledgements

First of all, I would like to thank my supervisor, Rainer Timm. Thank you for all the suggestions and guidance throughout this year. You are the kindest supervisor I could ever have. Your supportive feedbacks warm my heart and cheer me up every time.

I would also thank my co-supervisor, Rohit Yadav. You are a patient teacher and a nice friend to me. My STM and XPS skills mostly come from you. I really enjoy the lab time and mini-lecture time with you.

And I should express my gratitude towards all the members of the STM group. Especially Yi, every time I turned to you for help, I got to learn new skills. I will never forget the "wow" moments you gave me in the lab. I also got help from Sandra, who answers whenever I am in need. Yen-Po also hinted at some lab tricks to me when he was still in the division. Frankly, I am still regretting that I did not ask him to scan with me for some time. And Estephania, I quite enjoy the UHV work with you. Last but not least, the fika at the meeting on Wednesdays is a good memory for me.

There are nice people I met in Lund: Huaiyu, thank you for inviting me to your cozy home and giving me so much useful advice. Ruolin, Yuanyuan, and Qi, the weekly dinner party we held is my most precious weekend memory in Lund. All members at Yue-Han's house, I can never forget the peaceful evenings I spent with you. Varun, I miss the Indian cuisine at your place so much! And In-Pyo, I have a very vague memory about how we've become closer friends when you left Lund. I would assume that life in Sundsvall is quite boring, haha.

In the end,

to Lili: 我们就快要过上好日子了啦!

to my parents: 阿爸，阿妈，作为你们的儿子，我非常的的幸运。在人生的每个节点，你们都给我了充分的自由和支持。我爱你们!

Contents

1 Introduction

Semiconductor materials are a fundamental component of modern devices and play a crucial role in various fields, including electronics, telecommunications, and computing. They are materials with properties lying between conductors and insulators. The properties enable the control and manipulation of electrons to create electronic devices such as diodes and transistors, which are the building blocks of modern electronics.

III-V semiconductors are a class of materials composed of elements from group III and group V of the periodic table, e.g. gallium arsenide (GaAs), indium phosphide (InP), and gallium nitride (GaN). Compared to the commonly used semiconductor material silicon (Si), III-V semiconductors possess admirable electronic properties, such as direct, tunable bandgaps, higher charge carrier mobility, and customized crystal structure.

Among all III-V semiconductors, indium antimonide (InSb), the focus of this study, has the largest electron mobility($7.7 \cdot 10^4 cm^2 V^{-1} s^{-1}$). Other unique properties include a small electron effective mass, a narrow band gap ($0.17\ eV$), ample hole mobility ($850 \cdot 10^4 cm^2 V^{-1} s^{-1}$) [1], and a strong spin-orbit coupling [2]. These properties make InSb a promising material for infrared detectors [3], high-speed field effect transistors [4], spintronics [5], and topological superconducting quantum devices [6].

The properties of III-V semiconductors can be modified by adding other elements to them. Recently alloys with high bismuth (Bi) content have received increasing attention [7]. Bi can enhance spin-orbit coupling and reduce the band gap of the III-V-Bi alloys [8], and can also induce nontrivial topological properties [9]. However, III-V semiconductor alloy with high Bi content has a high lattice mismatch, since Bi is the largest atom among group V elements.

A different approach is to incorporate Bi into the III-V surface by Bi deposition, which is evaporating Bi onto the sample surface to form a thin layer. Nowadays, with the downsizing of electronic devices, surface properties become crucial for the functionality of nano-devices. Surface properties are different from that of the bulk part. With dangling bonds, the surface tends to undergo reconstruction to minimize surface energy. Therefore, investigating surface modification is important for future device applications.

Here, I want to deposit Bi on clean InSb surfaces and evaluate the resulting structure. First, I need to prepare and characterize clean InSb surfaces, so that I can compare them to the surface modifications induced by the deposited Bi, and understand the formation of thin Bi layers during the following deposition procedures. I want to apply different sample temperatures during the deposition process, since it influences the growth of the Bi layer on the surface. In addition, I want to see how annealing affects the deposited Bi layer.

For these investigations, we apply two highly surface-sensitive techniques: Scanning tunneling microscopy (STM) and X-ray photoelectron spectroscopy (XPS). STM allows characterizing surface topography at the atomic scale, while XPS can probe the chemical information on the surface. All experiments were performed in ultrahigh vacuum (UHV) conditions.

In this thesis, InSb(111)A/B surfaces are the host material. At our home lab, with STM, we investigated the surface reconstructions on clean surfaces, and the Bi adsorption behavior of the surfaces upon Bi deposition; with XPS performed at the MAX IV Laboratory, we studied the elemental information and bonding configuration of In, Sb, and Bi on the surface, which went through a sequence of surface treatments and Bi depositions.

2 Indium Antimonide (InSb)

InSb crystals adopt the cubic zinc blende (Zb) structure, as shown in Fig. 2.1(a). In the Zb structure, the In and Sb atoms occupy alternating positions in a face-centered cubic lattice. It can be considered as a superposition of two basic face-centered cubic lattices, with one having a shift of [1/4 1/4 1/4]. Every In atom is surrounded by four Sb atoms at the corners of a tetrahedron, and every Sb atom is surrounded by four In atoms in an identical configuration.

The lattice parameter at 298 K is $a = 0.648nm$ [10].

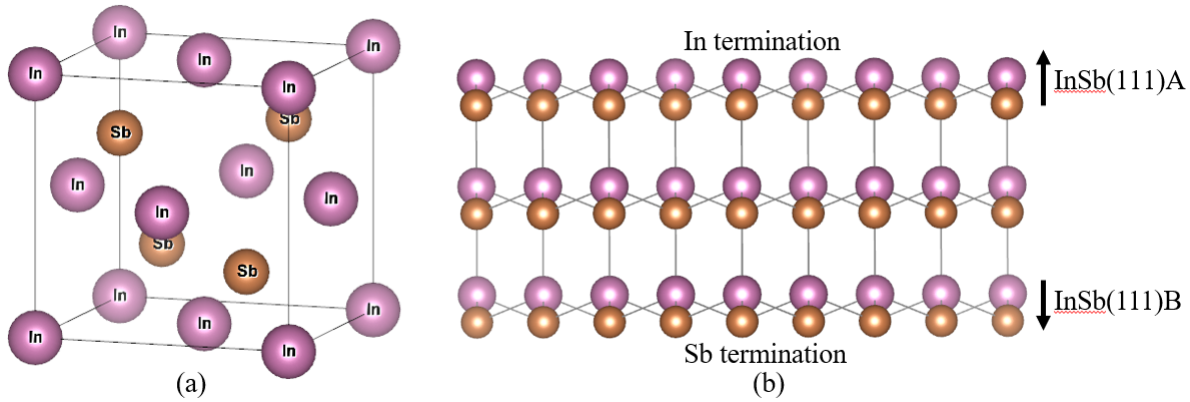

Figure 2.1: (a) A cubic cell of zinc blende structure of bulk InSb crystal; (b) Side view of the InSb(111) slab. The figure is made with the software VESTA.

InSb(111) surfaces are polarized, therefore have 2 types: (111)A and (111)B. As shown in Fig. 2.1, the (111)A surface is terminated with In atoms, while the (111)B surface is terminated with Sb atoms. For an InSb(111) slab, they are on the opposite side of each other.

The (111) surface lattice parameter is $a_0 = a/\sqrt{2} = 0.458nm$. One InSb double-layer (DL) consisting of one layer of In and one layer of Sb has a height of $d = a/\sqrt{3} = 0.374nm$.

3 Scanning Tunneling Microscopy

Scanning Tunneling Microscopy (STM) is a powerful technique in nanotechnology that allows the characterization of material surfaces at the atomic scale. It was developed by G. Binnig and H. Rohrer in 1981 [11], and they were awarded the Nobel Prize in Physics soon in 1986. STM can reveal both the topographical and electronic properties of the materials.

The simplified idea of STM is to use a sharp metal tip, which is in very close distance to the sample, but not touching it, to scan across the sample. With an applied bias voltage, a local tunneling current can be induced. By collecting data measured from each spot, one can create a 2-D map of the sample. The core tip-sample interaction is the quantum mechanical tunneling effect.

3.1 Theory

As the sharp metal tip approaches very close (a few nm) to a sample surface, the scale is reduced to where quantum mechanics dominates. With a wave-like behavior, an electron is possible to propagate through an energy barrier, even if the kinetic energy is less than the barrier energy. The non-negligible tunneling current between the tip and sample can reveal the sample properties.

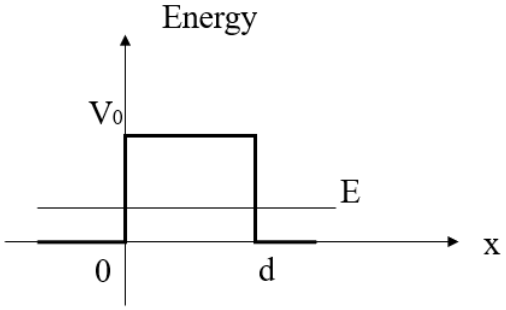

Figure 3.1: A 1-D finite square barrier.

The simplest illustration is shown in Fig. 3.1: an electron in a 1-D finite square well with a potential barrier V_0. The solution of the time-independent Schrödinger equation is:

$$\psi(x) = \psi(0) \cdot e^{\frac{x}{\hbar} \cdot \sqrt{2m(V_0 - E)}} \tag{3.1}$$

Where m is the electron mass, $\hbar$ is the reduced Planck constant, and E is the energy of the electron wave function. Consider the tunneling intensity as:

$$T = \frac{|\psi(d)|^2}{|\psi(0)|^2} = e^{\frac{-2d}{\hbar}\cdot\sqrt{2m(V_0-E)}} \approx e^{\frac{-2d}{\hbar}\cdot\sqrt{2mV_0}} \tag{3.2}$$

Where we assume $V_0 \gg E$. It is clear that T is exponentially dependent on d. In the STM schema, it tells: as the distance between the tip and sample surface decreases, the tunneling current increases exponentially.

Based on Bardeen's formalism, by considering all possible energy eigenstates, the net tunneling current is obtained as [12]:

$$I_{tot} = \frac{4\pi}{\hbar}\int_{E_F-eV}^{E_F} \rho_s(\varepsilon+eV) f_s(\varepsilon+eV)|M|^2 \rho_t(\varepsilon)\left[1-f_t(\varepsilon)\right] d\varepsilon \tag{3.3}$$

Where t and s represent the tip and the sample, respectively. ρ is the local density of states (LDOS); e is the charge of an electron; V is the tunneling voltage; M is the tunneling matrix; f is the Fermi distribution, which is:

$$f(\varepsilon) = \frac{1}{1+e^{(\varepsilon-E_F)/kT}} \tag{3.4}$$

To simplify the formula 3.3, we can apply Tersoff-Hamann approximation [13]: the tip has a circular apex and an s-type wave function; ρ_t remains constant; M is expanded in Bloch surface waves; assuming the temperature is low, the Fermi distribution is a step function. When the sample is metallic, V can be assumed small and the integral over eV can be approximated with a linear dependence on V. The resulting tunneling current is proportional to:

$$I_{tot} \propto V \cdot \rho_s\left(E_F\right) \cdot \rho_t\left(E_F\right) \cdot e^{\frac{-2d}{\hbar}\cdot\sqrt{2mV}} \tag{3.5}$$

While the tip-sample distance d is fixed, the tunneling current is proportional to the bias voltage V and $\rho_t\left(E_F\right)$, the LDOS of the sample at the position of the STM tip.

With semiconductor samples, the small voltage approximation fails. Instead, the tunneling current is proportional to the integrated LDOS of the sample:

$$I_{tot} \propto \rho_t \int_0^{eV} \rho_s\left(E_F+\varepsilon\right) d\varepsilon \tag{3.6}$$

However, the Tersoff-Hamann approach has a limitation in the details of the tip. The shape and the electronic state of the tip are not taken into account. In experiments, the images generated are the convolution of tip shape and sample topography. The valence resulting shell of a tungsten tip used in this study is d-type rather than s-type.

As indicated in the integral, the bias voltage V plays an important part by changing the Fermi level. Fig. 3.2 shows the schema of filled-state and empty-state imaging of

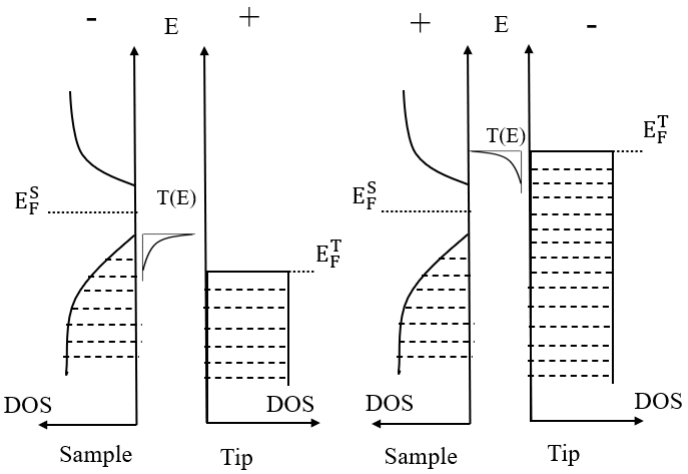

Figure 3.2: The left figure: filled state imaging, with a negative sample bias. The right figure: empty state imaging, with a positive sample bias.

semiconductors. For a negative sample bias, the Fermi level of the sample is higher than that of the tip. Therefore the electrons tunnel from the filled states of the sample to the empty states of the tip, indicating the filled state information of the sample. While for a positive sample bias, the electrons tunnel from the filled states of the tip to the empty states of the sample, indicating the empty state information of the sample. When imaging III-V compound semiconductor components in this study, they are In and Sb, the contrast is highly dependent on the bias voltage. The bias-dependent contrast is due to dangling bonds at the surface: There are empty dangling bonds (empty orbitals) located at the group-III atoms, while there are filled dangling bonds (orbitals with two electrons) located at the group-V atoms. Therefore in empty-state imaging, the tunneling current of In is higher than that of Sb. In the image, In atoms are bright dots. On the other hand, Sb atoms are bright dots in filled-state imaging.

3.2 Instrument Setup and Probe Tip

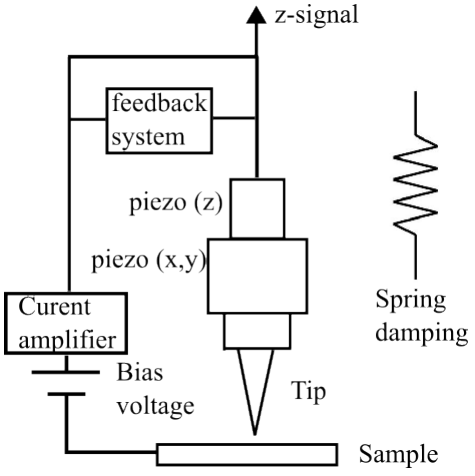

Figure 3.3: STM setup.

The instrument setup of STM is illustrated in Fig. 3.3. Piezoelectric material enables the atomic-scale movement of the tip. The horizontal piezo motors (x,y) control the tip to move from spot to spot on the sample surface, which is the scanning process. The STM can operate in constant height or in constant current mode, and the latter is used in this study. With the electronic feedback system, the vertical piezo motor (z) can adjust the height to keep the current constant. The movement of the tip in the vertical direction, the z-signal, is recorded to indicate the topographical information of the surface. Since the tip moves within atomic scale, external vibrations from the environment must be reduced. The vibration-damping system consists of springs that suspend the scanning platform.

An ultrahigh vacuum (UHV) environment is needed for STM operation. The main reason is to prevent the sample from surface modification like oxidation. In this study, the pressure in the STM chamber remains at low 10^{-9} mbar.

The shape and the conductivity of the tip play a crucial part in STM measurements. To prepare an STM tip, we use the electrochemical etching process: a 0.3 mm tungsten (W) wire is dipped into sodium hydroxide solution (NaOH, 2mol/liter). When a voltage (in our case, 4 - 9 V) is applied between the wire and a stainless steel counter electrode, the wire gets thinner as the redox reaction turns tungsten into soluble tungsten oxide. This process is strongest at the solution/air interface. It continues until the bottom part of the wire drops and the remaining part ends in a conical shape with a sharp tip. The sharpness of the tip is important because the STM image is a convolution of the tip shape and the surface shape. Fig. 3.4(a,b) gives an example of a sharp tip and a blunt/bent tip.

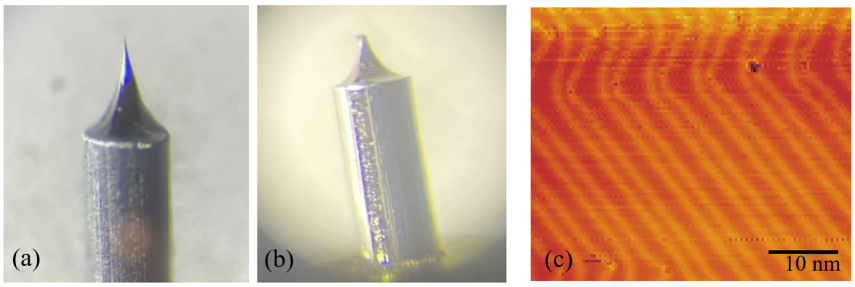

Figure 3.4: (a) A sharp tip; (b) A blunt/bent tip; (c)A STM image of herringbone structure on Au(111) surface.

To remove surface contaminations and oxide, in the UHV preparation chamber of the STM, the tip is sputtered with argon (Ar^+) for 30 minutes. The chamber pressure, acceleration voltage, and emission current are 2×10^{-6} mbar, 2 kV, and 10 mA, respectively.

The functionality of the tip can be examined by scanning a reference sample. The Au(111) surface exhibits a well-known herringbone structure, as shown in Fig. 3.4(c). One also can improve the conductivity of the tip by gently dipping the tip into the gold surface.

4 X-ray Photoelectron Spectroscopy

X-ray photoelectron spectroscopy (XPS) is a widely used technique to study surface chemistry including elemental information and bonding configuration. The idea of XPS originates from the photoelectric effect, which was discovered by Heinrich Hertz in 1885, and explained by Albert Einstein in 1905. In 1967, Kai Siegbahn developed the XPS technique, which was initially called electron spectroscopy for chemical analysis (ESCA) [14]. He was of course awarded the Nobel Prize in 1981.

In a nutshell, the principle of XPS is to inject photons and detect the out-coming electrons. The kinetics of the electrons contain chemical information about the sample surface. By scanning the kinetic energy of the detected electrons, the spectrum is obtained. In order to analyze the spectrum, one needs to understand how photons interact with matter.

4.1 Theory

X-rays are electromagnetic waves with wavelengths from 0.1 Å to 100 Å, and meanwhile are photons with energies from 100 eV to 100 keV. With high energies, the particle properties are often obvious. There are four processes involved in the interaction of X-rays with matter: photoelectric absorption, elastic scattering (Thomson scattering), Inelastic scattering (Compton scattering), and pair production. The photoelectric absorption process generates secondary electrons, phonons, and photons. The secondary electrons include photoelectrons and Auger electrons. In XPS, we focus on the photoelectron.

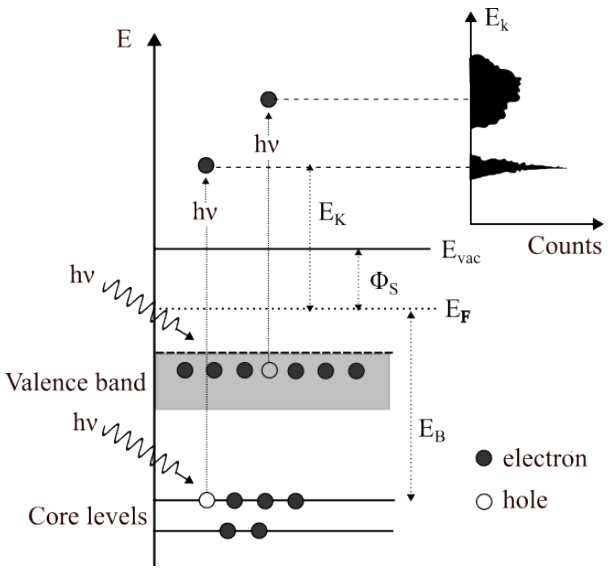

Figure 4.1: Energy diagram of the photoelectric effect.

The photoelectric effect is the basis of XPS. The process is illustrated in the energy diagram Fig. 4.1. A monochromatic photon beam with energy hv reaches the sample surface. A core-level electron absorbs the photon energy and gets excited to leave the sample surface. The photon energy hv has to be larger than $E_B + \Phi_S$, so that the photoelectron can be detected by the analyzer. E_B is the binding energy: the minimum energy required to excite an electron from the core level to the Fermi level. Φ_S is the sample work function: the energy needed to reach the vacuum level from the Fermi level. Then the photoelectron is detected in an electron energy analyzer, where the remaining photo energy, i.e. the kinetic energy E_K of the photoelectron, is detected. Therefore the binding energy E_B is obtained as a result of the energy conservation:

$$E_B = hv - E_k - \Phi_s \tag{4.1}$$

The electrons from the valence band also get excited to contribute to the spectrum. Since the valence electrons interact with the other valence electrons of neighboring atoms, they have energy bands. While the core-level electrons bound closer to the atomic nucleus display discrete energy states, which in the spectrum are sharp peaks centered at the binding energy positions.

The elemental information and bonding configuration of the sample surface is indicated by the binding energy of core-level electrons. Each core level of a given element has a distinct E_B. In addition, the chemical environment of the element affects E_B, causing the so-called chemical shift.

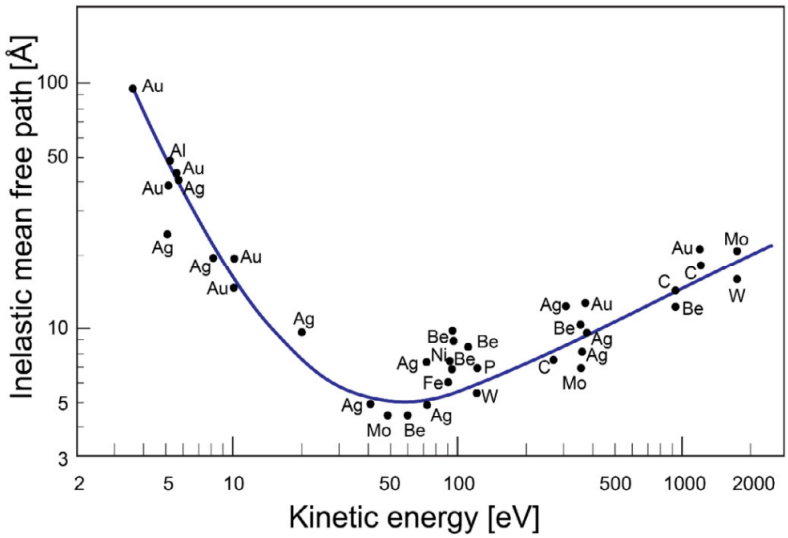

Figure 4.2: The inelastic mean free path (IMFP) dependency on the kinetic energy of electrons. Adapted from reference [15].

To demonstrate the surface sensitivity of XPS, we consider the inelastic mean free path (IMFP) of an electron. Inelastic electron-electron scattering dominates the attenuation process of an escaping electron. Electrons usually have a short IMFP and thus short escape depth from the sample surface. The IMFP mainly depends on the kinetic energy E_K of the electrons, as shown in Fig. 4.2. The IMFP obtains the minimum

(around 5 Å) at about 20 - 100 eV, and remains below 10 Å until about 500 eV. The electron escape depth is up to about three times as large as the IMFP. As mentioned in Chapter 2, the width of one InSb double-layer is 3.74 Å. This indicates that only the top few atomic layers of the sample surface are probed. In this study, soft X-rays with energy between 130 and 760 eV are used. By setting a proper photon energy range, the surface sensitivity of the core-level B_E can be obtained.

4.2 Spectrum Analysis

To understand the physical meanings of a spectrum and perform peak fitting, several important parameters are introduced below.

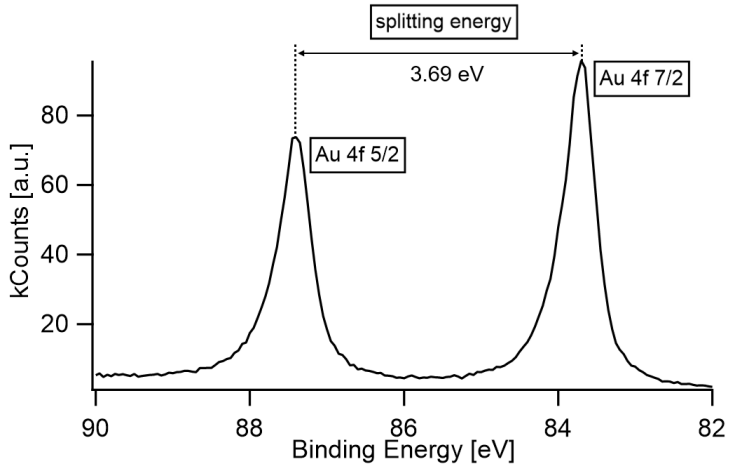

Figure 4.3: XPS spectrum of Au 4f.

An XPS spectrum of a specified core level of an element usually exhibits two peaks, the so-called spin-orbit splitting. The spectrum of Au 4f is shown in Fig. 4.3 as an example. "Au" is the element gold; "4" represents the core-shell principal quantum number $n = 4$. "f" indicates the orbital angular momentum number $l = 3$. The two peaks are due to the spin-orbit coupling and are called a doublet. For Au 4f, the spin angular momentum is $s = \pm 1/2$, thus the total angular momentum is $j = |l \pm s| = |3 \pm 1/2| = 5/2$ and $7/2$, corresponding to the peak Au $4f_{5/2}$ and Au $4f_{7/2}$ respectively. There are two parameters for a doublet:

Spin-orbit splitting energy is the energy difference between two peaks in the doublet. It is a fixed number for a specified core level of a specified element. For Au 4f, the spin-orbit splitting energy is 3.69 eV.

Spin-orbit split peak weight ratio is the intensity ratio of two peaks in the doublet. It is also a fixed number. Theoretically, it is 0.75 for 4f, because $4f_{5/2}$ has $2j + 1 = 6$ microstates, and $4f_{7/2}$ has 8 microstates. In practice, the value can deviate within a reasonable range.

A single peak is featured as a Voigt function, which is a convolution of a Gaussian function and a Lorentzian function. Thus, a single peak is characterized by the following

parameters:

Peak intensity is mainly dependent on the amount of the component. With suitable calibration, the relative change in the concentration of a component can be obtained.

Lorentzian width is related to the core hole lifetime. It is a fixed value for a specified core level, unrelated to the chemical environment.

Gaussian width is related to the instrumental factors and the crystalline quality. The value can change for the same core level.

Background formed by the secondary photoelectrons is subtracted with a linear function, for the purpose of peak fitting.

4.3 Synchrotron X-ray Sources at MAX IV

Synchrotron radiation facilities are built to produce X-rays of the highest quality. The X-ray sources have optimal brilliance which is ten orders of magnitude higher than that of laboratory sources, and the beam has a small focus down to tens of nanometers. The photon energy is not only highly monochromatic but also tunable. In XPS, this allows us to probe different core levels of interest.

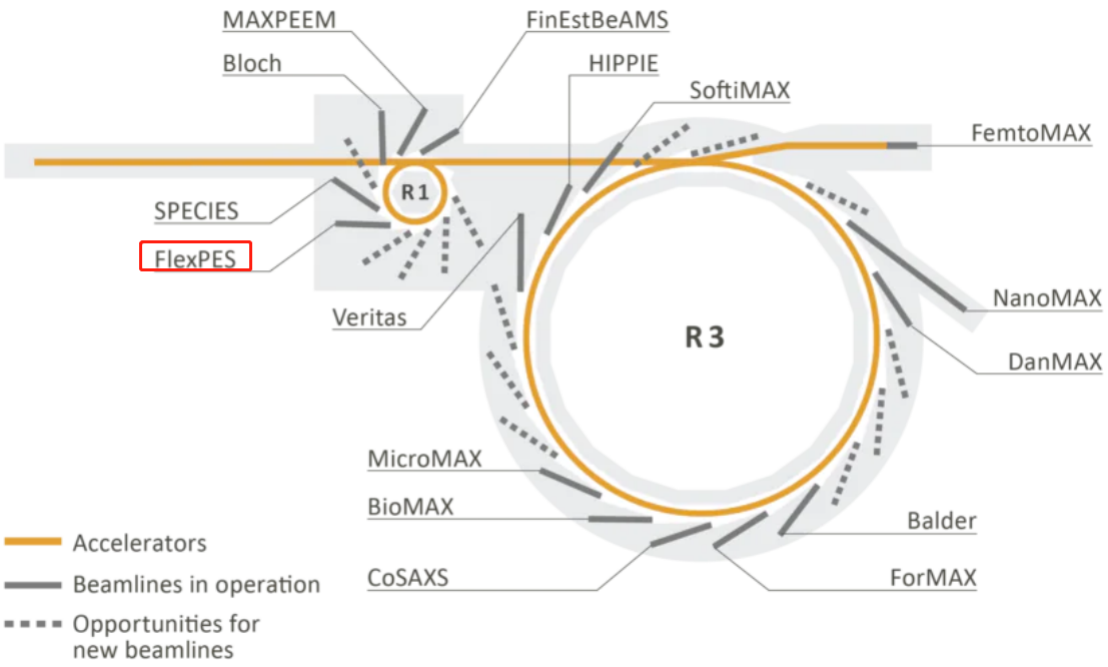

Figure 4.4: Schema of MAX IV. The beamlines are situated on the 1.5 GeV (R1) and 3 GeV (R3) storage rings. Adapted from reference [16].

MAX IV is a state-of-the-art 4^{th} generation synchrotron, located in Lund, Sweden. The schema is shown in Fig. 4.4. Electrons generated by the electron gun are accelerated by the linear accelerator up to a kinetic energy of 1.5 GeV or 3.0 GeV, and then circulate at quasi-relativistic speeds in the storage rings. There are specially arranged

magnetic devices to keep electrons traveling in the rings. To generate the radiation, the electrons are induced to oscillate as going through an undulator, which consists of periodic arrays of magnets. The generated X-ray beams are then coupled into the beamline, where there are optics to monochromatize and focus the beams. Finally, the resulting X-ray beam is put to use at the experimental station.

MAX IV provides access to 16 beamlines for various purposes. The beamline used in this study is FlexPES (Flexible PhotoElectron Spectroscopy) [17], which provides X-rays in the energy range of 43 - 1550 eV. The chambers are kept at UHV to allow the XPS to work and also to protect the samples.

4.4 Low Energy Electron Diffraction

Low Energy Electron Diffraction (LEED) is a common technique used in surface science and materials research to study the structure and arrangement of atoms on the surface. There is a LEED setup built in the XPS setup, and we used it to examine the quality of prepared InSb(111)A/B surfaces before XPS measurements.

In LEED, a beam of electrons with energies typically ranging from a few eV to a few hundred eV is generated and directed at the sample surface at a shallow angle. The incident electrons interact with the atoms on the surface and undergo scattering, resulting in diffraction. The diffracted electrons form a pattern that depends on the arrangement and periodicity of the surface atoms. The pattern is basically the reciprocal lattice of the surface lattice. Therefore, surface symmetry can be determined from the pattern.

5 Sample Preparations

In this study, the samples were crystal pieces cut from an epi-ready InSb (111) wafer, which was n-doped with a Te concentration of (3-8)x10^{14} cm^{-3}. Atomic hydrogen treatment was applied to clean the surface, and the Bi deposition was performed with an evaporator.

5.1 Atomic Hydrogen Cleaning Process

Atomic hydrogen treatment [18] was applied to remove oxides and contamination on the surface of the sample. Compared to more commonly used argon sputtering methods, it is mild, causing fewer surface defects on the substrate, yet efficient enough.

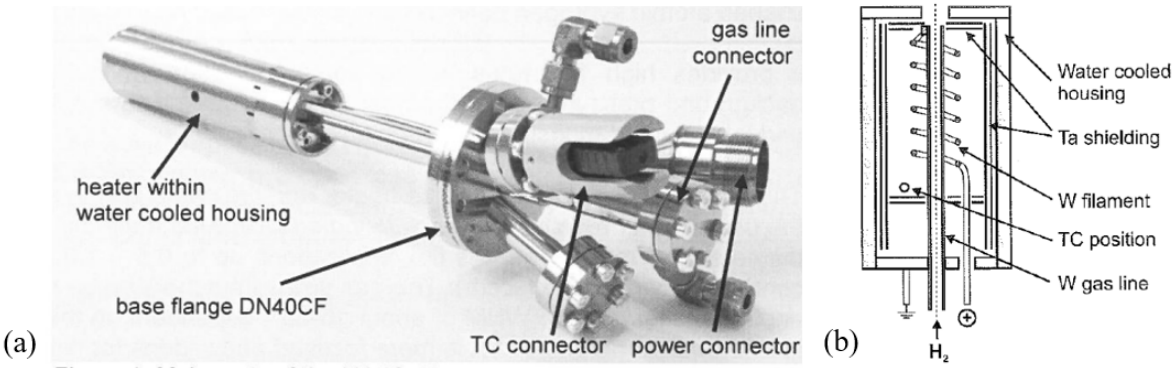

Figure 5.1: (a) Main parts of the hydrogen cracker, where TC is abbreviated for thermocouple. (b) The internal structure of the heater. Adapted from reference [19]

As shown in Fig. 5.1 (a), a hydrogen cracker consists of a power connector to supply DC power, a gas line connector to introduce H_2 gas flow, a thermocouple (TC) connector, water cooling connectors, and the core heater part. As shown in Fig. 5.1 (b), the H_2 gas flows through a thin tungsten(W) capillary surrounded by a W filament. The capillary is heated by the W filament. With operation temperatures up to 2100 °C, H_2 molecules are dissociated to atomic hydrogen, which is called thermal cracking of H_2 molecules. A narrow-angle hydrogen gas beam is ejected into the experiment chamber aiming for the sample surface. To reduce the native oxide on the sample surface, the H_2 molecules are not reactive enough, but H atoms are highly reactive, which can remove the surface oxide with increased sample temperature.

It is worth noticing that the TC position is next to the bottom of the heater, without direct contact with the W tube. Therefore the measured TC temperature can be significantly different from the true temperature of the W tube.

During operation, the sample was annealed at 360 to 380 °C, and the filament of the

hydrogen cracker was at 1700 °C. The background pressure of the experiment chamber was at 2 to 3 $\times 10^{-6}$ mbar. One treatment lasted for 30 minutes.

5.2 Bismuth (Bi) Deposition Process

The Bi evaporator was used to perform the Bi deposition onto the sample surface.

The main features of the Bi evaporator are shown in Fig. 5.2. The core part is the crucible, where solid Bi is melted and evaporated into the experiment chamber. Then Bi atoms adsorb on the sample surface. The crucible is heated by a Ta-wire filament. The temperature is measured by two pairs of thermocouples. The Ta shutter plate is used to shield the exit while not in operation.

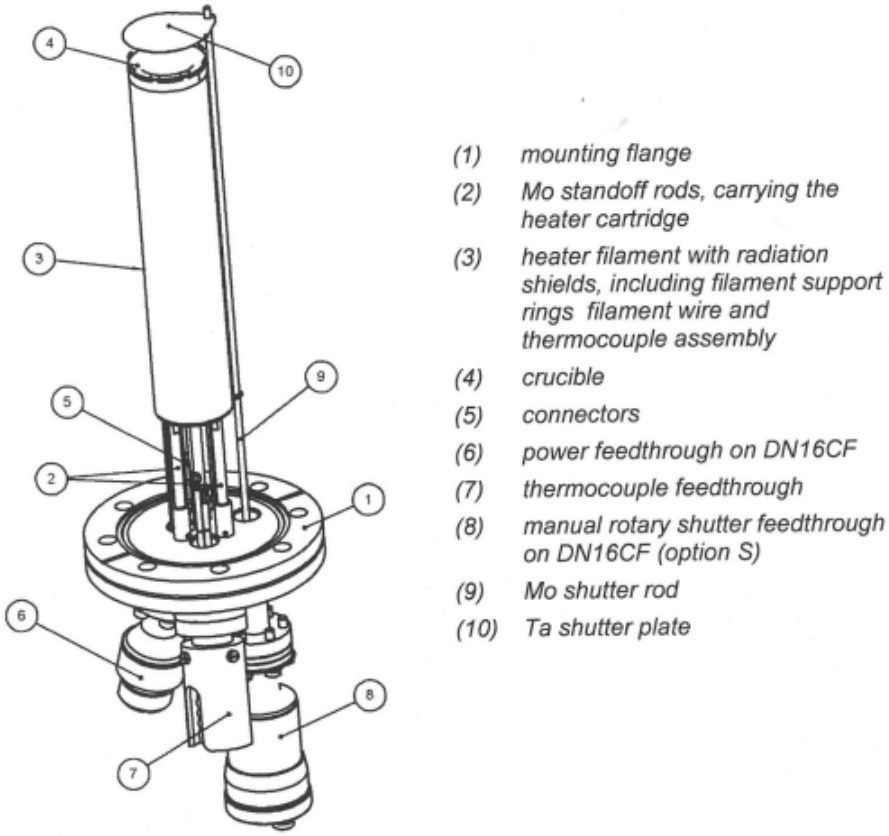

Figure 5.2: Overview of basic features of the Bi evaporator. Adapted from reference [20].

During a Bi deposition process, the liquid Bi in the crucible was heated at 400 °C (the melting point of Bi is 271.4 °C). The sample surface was facing the Bi source while in operation. One treatment lasted for 15 minutes.

The sample was kept at a specified temperature during a deposition process. We chose two different sample temperatures, 250 °C and room temperature (RT). I call the former *regular Bi deposition* and the latter *RT Bi deposition*. We chose 250 °C because it allows Bi layers to grow moderately on the sample surface. With higher

temperatures, Bi layers hardly grow. While with lower temperatures, Bi layers grow too fast. RT Bi deposition was intentionally performed to grow excessive Bi layers.

Annealing the sample at 250 °C for 10 minutes is called an annealing process.

In the STM experiment, the sample went through a regular Bi deposition for 15 minutes.

In the XPS experiment, the sample underwent a sequence of Bi depositions:

(1) First regular Bi deposition for 15 minutes;

(2) Second regular Bi deposition for 15 minutes;

(3) Third regular Bi deposition for 15 minutes;

(4) RT Bi deposition for 30 minutes.

And in the last, the sample was annealed at 250 °C for 10 minutes. This process was used for evaporating the excessive Bi layers, which were added by the RT Bi deposition process.

6 STM Results and Discussion

After atomic hydrogen treatment, the InSb(111)A/B surface without an oxidation layer is obtained. The clean surface is scanned with negative sample bias voltage, i.e. filled state imaging.

6.1 Clean Surface of InSb(111)A

As shown in Fig. 6.1 (a), an atomically resolved image of the clean InSb(111)A surface is obtained. The distribution of the Sb atoms matches that of the theoretical InSb(111)A surface shown in Fig.6.3 (a). The measured lattice constant is 0.5 nm, which is close to the theoretical value $a_0 = 0.458$ nm.

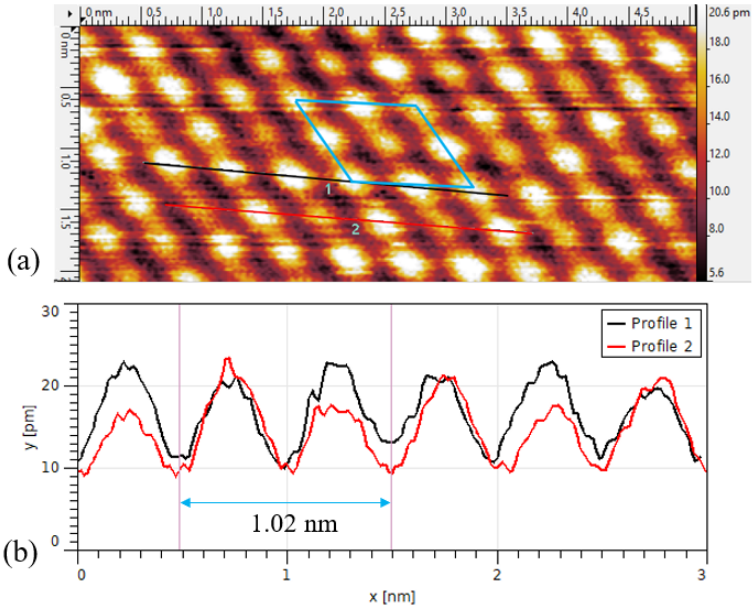

Figure 6.1: (a) Filled-state imaging of InSb(111)A, with bias voltage V_{bias} = - 3 V and tunneling current I_t = 2420 pA. The blue parallelogram indicates the 2×2 reconstruction unit. (b) Line profiles of the black and red lines in (a).

However, the image7

d Sb atoms are not all equivalent. As illustrated in Fig. 6.1 (b), line profile 1 shows an approximately even height at each Sb atom, while line profile 2 indicates that the peak is evidently lower at every other Sb atom. This tells us there are two species of Sb atoms on the surface. Recall that the constant current mode is applied in this study, the Sb with a lower density of states (DOS) requires the tip to approach closer to get a larger tunneling current. Therefore, the "darker" Sb atoms with lower peak profiles have a smaller DOS, indicating a different bonding configuration from the other "brighter" Sb atoms.

In order to minimize the surface energy, the surface atoms are usually rearranged to form periodic complex constructions. This is called the *surface reconstruction*. The periodicity is expressed as a multiple of the original surface lattice constant. In Fig. 6.1(a), the (2×2) reconstruction is indicated by the equilateral parallelogram with an angle of 60 degrees. As displayed in Fig. 6.1 (b), the measured reconstruction size is 1.02 nm, close to the expected value $2a_0 = 0.916$ nm.

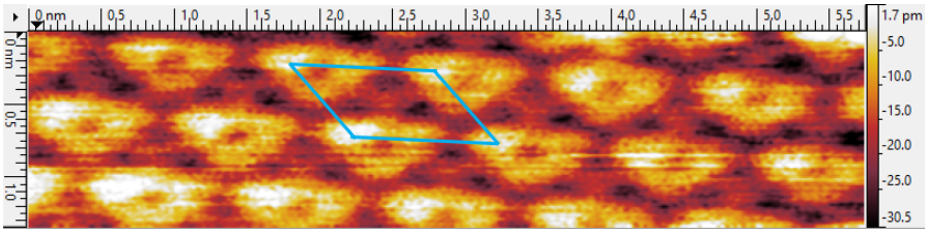

Figure 6.2: Filled-state imaging of InSb(111)A, with bias voltage V_{bias} = - 2.1 V and tunneling current I_t = 2770 pA. The blue parallelogram indicates the 2 × 2 reconstruction unit.

The (2×2) reconstruction is more evident in Fig. 6.2, as framed by the blue parallelogram. The contrast difference between Fig. 6.1 and Fig. 6.2 is caused by the bias voltage difference and possibly the change in the electrical states of the tip. First, we exclude the latter influence factor in the analysis. Recall equation (3.6) in Chapter 3.1, we know that with a higher bias voltage, the integral extends to LDOS at lower energy levels, thus revealing DOS information there. The Sb species with dim dots at -2.1 V get higher contrast at -3 V, which implies the Sb species with dim dots has much more states in the range of $E_F - 2.1eV$ to $E_F - 3.0eV$ than that of the Sb species with bright dots. This is actually the principle of scanning tunneling spectroscopy (STM), which detects the DOS information. The change in the electrical states of the tip is however complicated, (which will be shown in Fig. 6.5), because the tip can experience picking up or dropping unknown atoms, and shape change. The apparent distortion of the reconstruction unit is due to the piezo creep. That is a time delay in the deformation of the piezo material which causes the tip position to drift. It usually happens after moving the tip to another scanning region and fades away over time.

An experienced STM experimentalist may find the tunneling current I_t = 2770 pA unrealistically high. The reason behind it is the tip used. This tip was found to be severely bent. It is exactly the tip shown in Fig. 3.4 (b).

Since Sb atoms are located exactly the same as the original surface lattice, the educated guess to explain why there are two species of Sb atoms is: there is a rearrangement of In atoms. In order to determine the atomic structure of (2×2) reconstruction of InSb(111)A surface, empty state imaging is needed to examine In atoms. However, the scanning was unstable with a positive sample bias. Thus there is a lack of this important data.

Turning to literature, it turns out that the (2×2) reconstruction of InSb(111)A has been well explained by the In-vacancy buckling model [21]. As shown in Fig. 6.3 (b), in every (2x2) reconstruction unit, there is a lack of an In atom. The positions of the remaining atoms shall deviate from their ideal positions due to the relaxation to minimize the surface energy, which is not shown in the figure. There are two species of

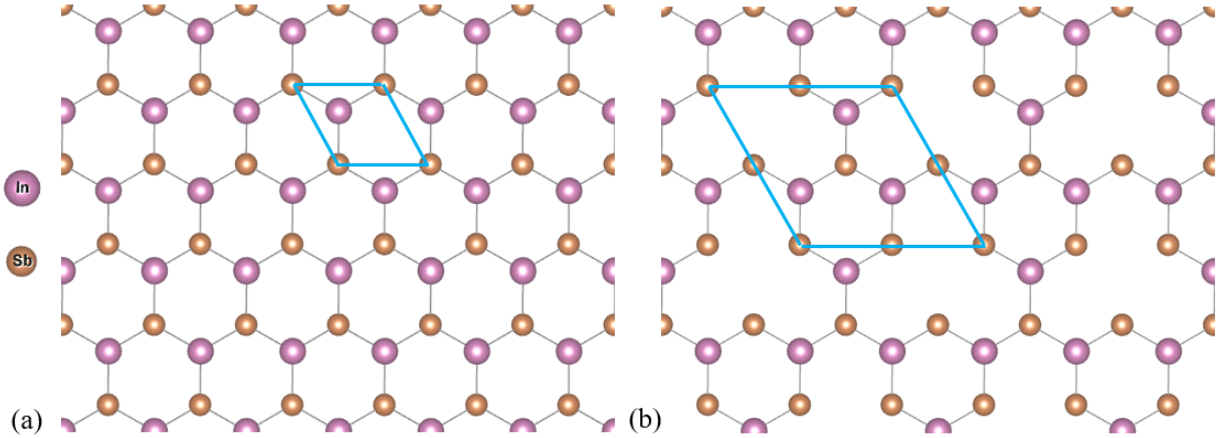

Figure 6.3: Atomic structure of the InSb(111)A surface (a) without reconstruction; (b) with 2×2 reconstruction. The blue parallelograms indicate (a) the original (111) surface lattice unit and (b) 2×2 reconstruction unit.

Sb atoms: the majority are bonded to two adjacent In atoms, while the minority, which is represented as the center Sb atom in the blue frame, is bonded to three adjacent In atoms. The former has one more extra dangling bond than the latter. This provides an extra filled state, i.e. higher DOS. Therefore it is the brighter atom in the STM images, as can be seen in Fig. 6.1 and Fig. 6.2.

Another surface reconstruction type of InSb(111)A surface is the $(2\sqrt{3} \times 2\sqrt{3})$ reconstruction. which is produced under Sb-rich synthesis conditions [21, 22, 23]. There is evidence showing that the (2×2) and $(2\sqrt{3} \times 2\sqrt{3})$ reconstructions can coexist [24]. It suggests that the $(2\sqrt{3} \times 2\sqrt{3})$ reconstruction is formed by Sb trimers sitting on the In vacancy sites of the (2×2) reconstruction. By annealing, the $(2\sqrt{3} \times 2\sqrt{3})$ reconstruction can degenerate to (2×2) reconstruction, with the Sb-trimer atoms evapeorated. The fact is that all III-Sb (111)A surfaces can exhibit reconstructions with a periodicity $(2\sqrt{3} \times 2\sqrt{3})$, but due to different physical origins [22].

In this study, we only observed (2×2) reconstructions, not $(2\sqrt{3} \times 2\sqrt{3})$. This could be due to the annealing process for cleaning. The $(2\sqrt{3} \times 2\sqrt{3})$ reconstructions shall be annealed away, if there were any.

6.2 Clean Surface of InSb(111)B

As the scanning result shown in Fig. 6.4 (a), the clean InSb(111)B surface shows a highly periodic surface structure. Consider every bright dot as a unit, the measured period is 1.45 nm, which is close to $3a_0 = 1.37$ nm. Therefore this is a (3×3) surface reconstruction. The bright dots are not single atoms but a complex aggregation of atoms. There are defects as missing units, which are emphasized in Fig. 6.4 as dotted yellow circles. The big bright spot is a surface contaminant, which could result in the disarrangement of the nearby units. The terraces are usually equilateral triangles, as shown in Fig. 6.4 and Fig. 6.5, and the terrace edges are along $< 110 >$ directions, because Zb crystals cleave naturally along the 110 planes [25]. The height profile along

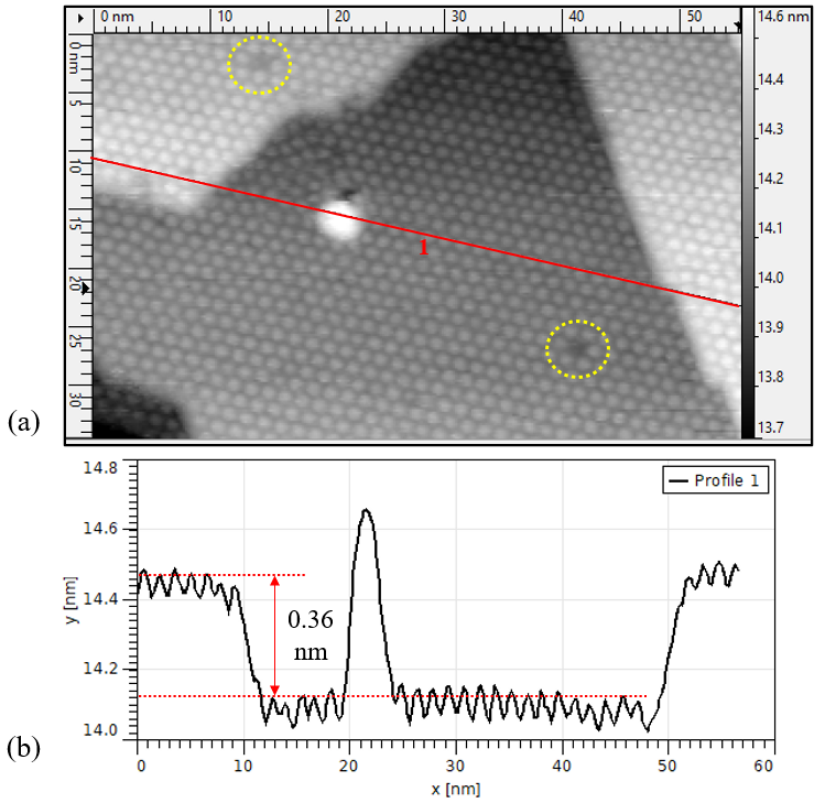

Figure 6.4: (a) Filled-state imaging of InSb(111)B, with bias voltage V_{bias} = - 2.5 V and tunneling current I_t = 100 pA. (b) The line profile along the red line in (a).

the red line is shown in Fig. 6.4 (b). The height of the terrace is 0.36 nm, indicating that it is one InSb double-layer (d = 0.374 nm) as mentioned in Chapter 2.

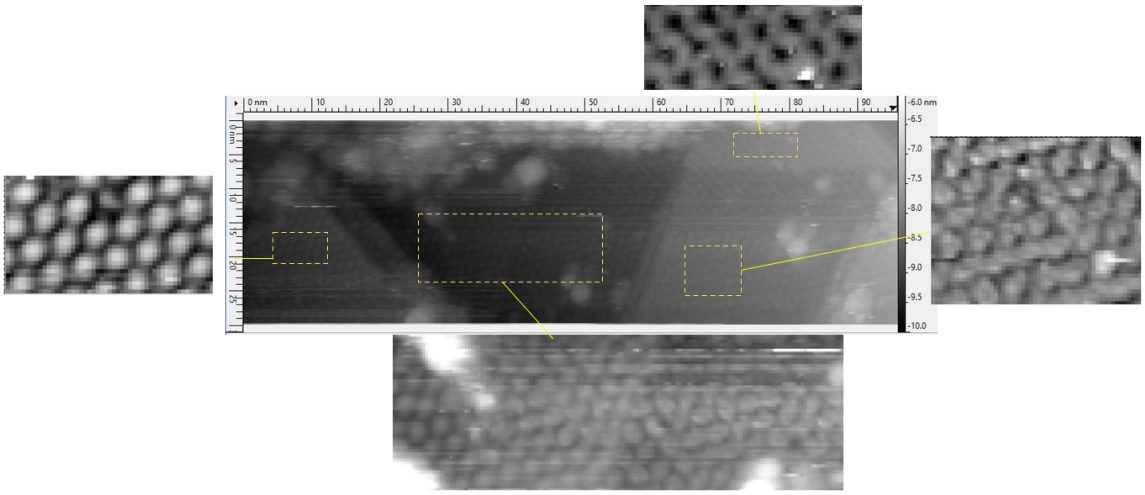

Figure 6.5: Filled-state imaging of InSb(111)B, with bias voltage V_{bias} = - 3 V and tunneling current I_t = 110 pA. The magnified areas are framed with yellow dotted rectangles.

While measuring the period value of the surface reconstruction, the precision should be treated with caution. Not only the piezo creep can affect the value, but also different individual InSb(111)B samples deliver values with deviation, which is 1.39 to 1.57 nm

in this study. However, a good consistency of the measured value is observed on the same sample.

It is common that the tip experiences sudden changes during the scanning process. A big change like picking up or losing a considerable piece (e.g. 10 nm), can be seen from a steep rise or drop of the height signal. More subtle changes in the electric states of the tip, however, can affect the contrast of the reconstruction units. As illustrated in Fig. 6.5, with the same surface structure, different regions exhibit different appearances (the periodicity of the units is the same though). This is further proven by observation of different contracts of successive scannings at the same place. What is good is that some contrast with atomic resolution can reveal the structure of the reconstruction unit.

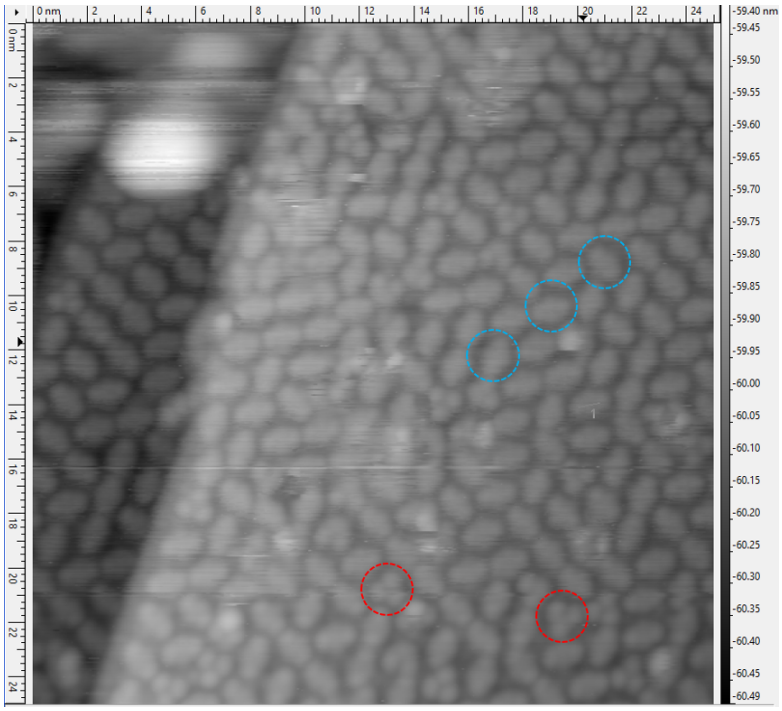

Figure 6.6: Filled-state imaging of InSb(111)B, with bias voltage V_{bias} = - 2.5 V and tunneling current I_t = 100 pA. α type and β type units of the (3×3) reconstruction are emphasized by dotted blue and red circles, respectively.

As shown in Fig. 6.6, there are two types of (3×3) reconstruction units, and they are randomly oriented with rotations of 60°. (1) α type is dominant in numbers, having an elongated shape. At two ends of it, there are two brighter dots, while in the middle it is smeared out. This suggests two or more Sb atoms in a α type unit. (2) β type has a more clear structure: three dots at the corners of an equilateral triangle. This tells three Sb atoms are in a β type unit. However, I did not manage to obtain the empty states imaging to map out the In atoms.

After a literature survey on the atomic structure of the reconstruction, I indentified that the hexamer structure model suggested by J. Wever [26] matches our STM result. As shown in Fig. 6.7, the hexamers are sitting on top of a complete InSb double layer, with a periodicity of $3a_0$. The α ring has a stoichiometry of In_4Sb_2. The two Sb atoms account for the two bright parts at both ends of the elongated shape in Fig. 6.6. The

beta α ring has a stoichiometry of In_3Sb_3, where the three Sb atoms in the triangular arrangement also explain the image well.

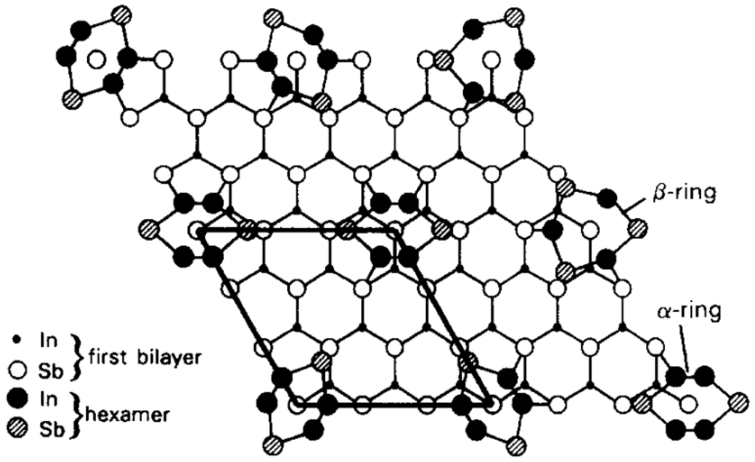

Figure 6.7: Top view of the hexamer structure model. The solid parallelogram shows the (3×3) unit cell. Adopted from reference [26].

The InSb(111)B surface also can exhibit a (2×2) reconstruction, where Sb trimers sit on the InSb double layer with a periodicity of $2a_0$ [21]. The comparison to the In-vacancy model of InSb(111)A - (2×2) reconstruction clearly shows the different polarity of A surface and B surface. One is the standard surface with a missing In atom per unit cell, the other one has extra Sb-trimers sitting on top.

It is worth noting that the (2×2) and (3×3) surface reconstructions of InSb(111)A/B clean surfaces are supported by the surface components identified in XPS spectra, and also verified by LEED. The details are in Chapter 7.

6.3 Bismuth (Bi) Deposition

Bismuth deposition was performed for 15 minutes on the clean InSb(111)A surface and InSb(111)B surface.

As shown in Fig. 6.8 (a), on the surface, atoms aggregate randomly to form amorphous piles. Although there are no obvious terraces visible in the STM image, steps in the height profile along the green line can still be recognized, as shown in Fig. 6.8 (b), to distinguish separate layers. Each step is about 0.7 nm high, which corresponds to twice the height as that of the terraces found on clean InSb(111)B (see Fig. 6.4).

Small clusters consisting of several Bi atoms are found on the piles. For example, in Fig. 6.8(c), a cluster of 4 Bi atoms is illustrated by a dotted blue frame. The distance between adjacent atoms is about 0.48 nm, which is close to the experimental lattice parameter at 298 K, a = 0.4546 nm, of bulk Bi [27].

The Bi deposition layer is so thick that no area of the exposed clean surface is found. At this point, it can only be speculated if the deposition time and thus the amount

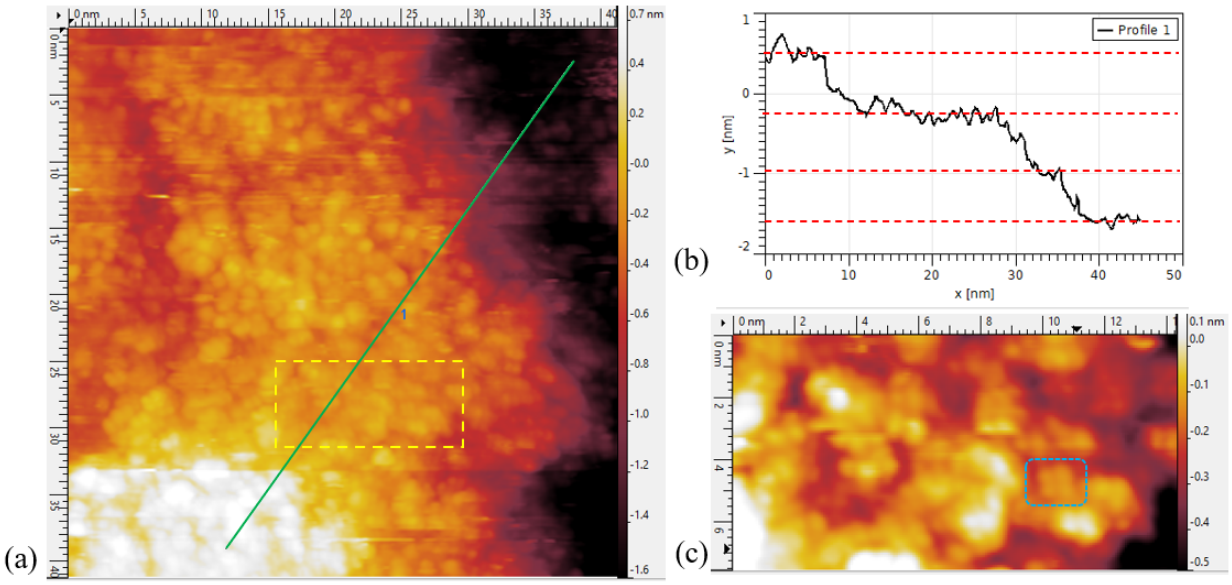

Figure 6.8: (a) Filled-state imaging of InSb(111)A with 15 minutes Bi deposition. Bias voltage V_{bias} = - 3.5 V and tunneling current I_t = 160 pA. (b) The line profile along the green line in (a). (c) The magnified image of the area framed by the dotted yellow rectangle in (a).

of deposited Bi was too high, or if the chosen deposition parameters do not allow the formation of a well-ordered Bi-containing layer. For the InSb(111)B surface with Bi deposition, as shown in Fig. 6.9, the scanning result shows similar features as those of InSb(111)A with Bi deposition.

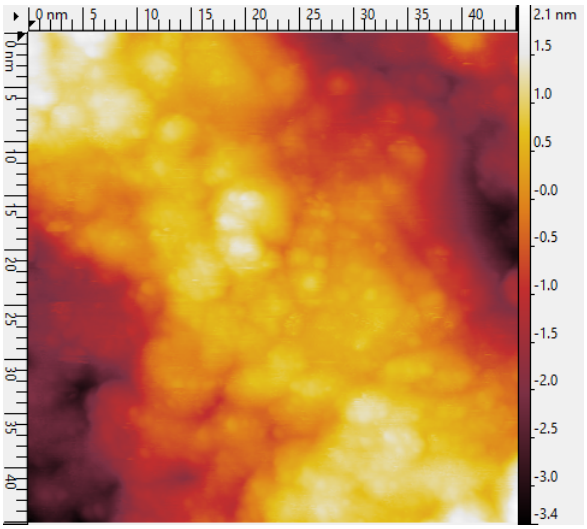

Figure 6.9: Filled-state imaging of InSb(111)B with 15 minutes Bi deposition. Bias voltage V_{bias} = - 3.2 V and tunneling current I_t = 150 pA.

If we in future experiments decrease the deposition time to make the Bi layer very thin, there could be some more interesting features other than boring amorphous piles. It is reported that Bi deposition on InSb(111)B surface can induce a Sierpiński-triangle-like fractal structure in Bi thin films [28].

During the STM experiments, a lot of time-consuming problems happened. The sample wafer was not satisfying. Due to mutual grinding among wafer pieces in the package, there was visible (and very likely invisible) crystal powder on the sample surface. This could result in the increasing difficulty of the scanning measurements. A new wafer has already been shipped to the division, and further investigations will be conducted. During my research, The UHV STM chamber was vented twice due to mechanical problems, which each time took weeks to fix. In addition, there was a leakage issue dwelling for months, which reduced the sample preservation time. It has already been fixed by leakage inspection with a mass spectrometer. Making and preparing new tips also required much time. Performing STM requires strategically correct patience, which takes time for one to gain.

7 XPS Results and Discussion

InSb(111)A and InSb(111)B have both been studied with XPS, and the results are discussed in this chapter. In most cases, the behavior of them is similar. Thus, I focus mainly on the spectra of InSb(111)A.

7.1 Overview Spectrum

Before going to the detailed spectra analysis of specified elements, it is necessary to take a rough look at the overall chemical information of the untreated native sample. With photon energy of 760 eV, the spectrum covers a large range of binding energy.

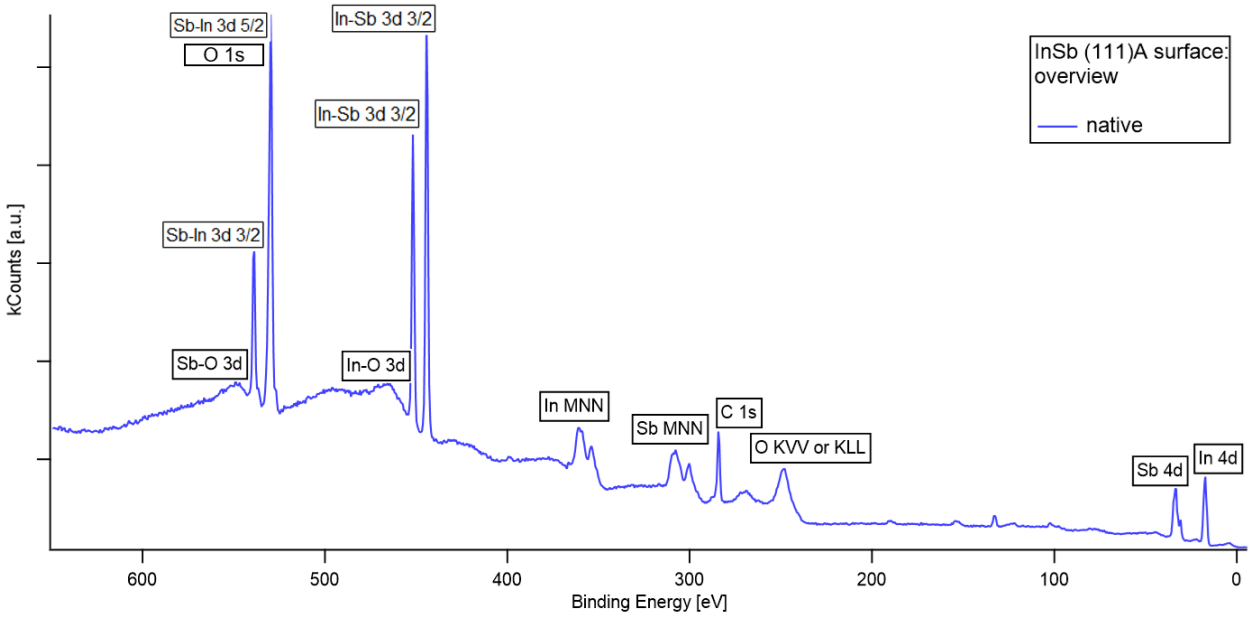

Figure 7.1: Overview XPS spectra of an uncleaned InSb(111)A sample. Photon energy is 760 eV.

To identify the peaks in the spectrum, I turned to the online NIST XPS Database[29], where energies of many photoelectron and Auger-electron spectral lines can be searched. The basic principle is first looking for the core level peaks of the elements of interest, then identifying other unknown peaks with Auger kinetic energy searching.

The overview spectrum is shown in 7.1. The peaks are labeled by the element and its bonding. For example, Sb-In is the peak of Sb with Sb-In bonds. The detected core levels of In and Sb are 4d and 3d. For 3d, the spin-orbit splitting between 3d 5/2 and 3d 3/2 is big enough to be resolved. Besides the sharp Sb-In and In-Sb peaks, the oxidation components with the chemical shift are also identified. Since the binding energy of O 1s is also in the energy range of overview, the peak at 530 eV is identified

to be an overlap of Sb 3d 5/2 and O 1s. The ratio between the Sb 3d 5/2 and 3/2 doublet is abnormally high, (the theoretical value is 1.5), indicating the existence of O 1s. The 4d case will be discussed in detail in the following sections. The Carbon (C) core level 1s is also detected, indicating the existence of surface contamination.

The other peaks are caused by auger electrons, which are electrons emitted when an inner-shell electron is ejected from an atom, and the resulting core hole is filled by an electron from a higher energy level. The notation rule can be found in [29]. In Fig. 7.1, In MNN, Sb MNN, O KVV/KLL are identified.

With lower photon energy, the surface sensitivity of XPS is higher. Therefore, for all the following spectra, a photon energy of 130 eV is used. The binding energy range of interest is from 13 to 40 eV, covering core levels In 4d, Sb 4d, and also Bi 5d which is not shown in the overview.

7.2 Removal of Oxide on the Surface

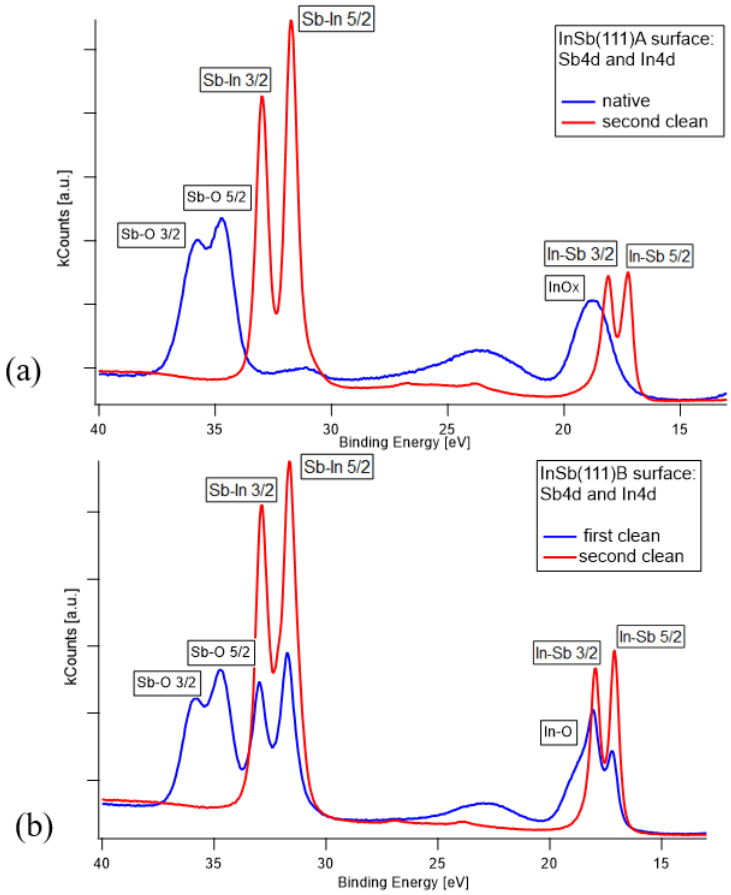

Figure 7.2: XPS spectra of (a) Sb 4d core level and In 4d core level before and after cleaning; the sample is InSb(111)A. (b) Sb 4d core level and In 4d core level after first cleaning and second cleaning; the sample is InSb(111)B. Photon energy is 130 eV for all spectra.

The untreated native sample surface was exposed to air before being put into the UHV

environment. Therefore, it has a thin layer of oxide, which is to be removed by the atomic hydrogen cleaning process. By examining the oxide components in the XPS spectra, one can decide if the surface is clean enough.

The comparison between the spectrum before and after oxide removal is shown in Fig. 7.2. In (a), the spectrum of the clean surface shows only peaks of Sb and In with In-Sb bonding configurations. While in the native spectrum, the Sb-O and In-O bonds prevail. This shows that XPS only probes a very thin layer on the surface. In (b), the spectrum of the partially cleaned surface possesses both, telling that the oxide is partially removed. Although it is obvious, it's worth noticing that the In-Sb 3/2 peak has a "shoulder" on the higher energy side, which is the In-O component superposed in it. This component observation method is applied throughout the XPS spectra analysis.

Low energy electron diffraction (LEED), which can reveal the crystal structure and surface symmetry by diffraction patterns, is also applied to examine the crystal quality of the (111) surface. As shown in Fig. 7.3, the bright dots show hexagonal symmetry, implying good surface quality. The less bright dots hinted by green arrows indicate (2×2) and (3×3) reconstructions on the InSb(111)A and InSb(111)B surface, respectively.

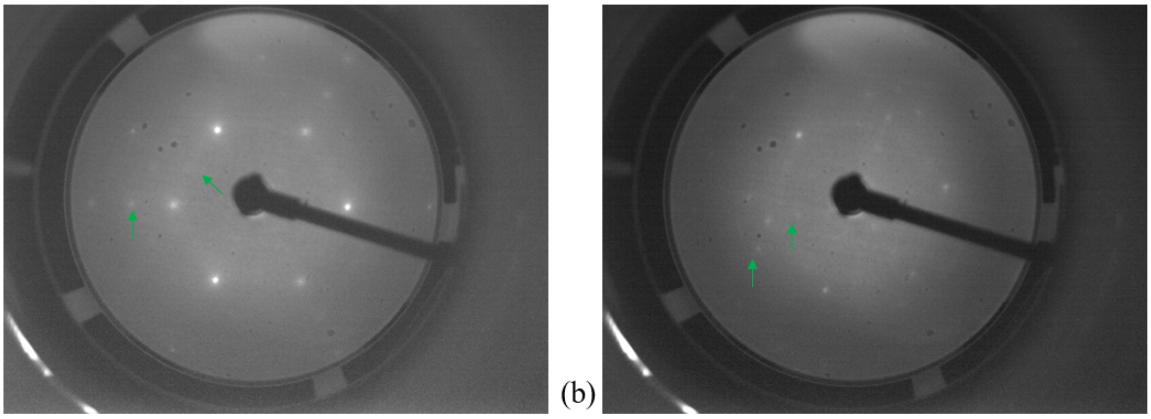

Figure 7.3: LEED patterns of second-cleaned (a) InSb(111)A surface and (b) InSb(111)B surface. The electron energies are 80 and 72 eV, respectively.

7.3 Spectra of In and Sb

In order to study the evolution of chemical information during the sequential treatments (which are elaborated on in Chapter 5), we need to calibrate the spectra measured after each treatment. From the previous experience in the group, the peak in In spectra remains almost the same during the process of treatments. So I calibrate the spectra by In-Sb 5/2 peaks: every spectrum is shifted in horizontal and vertical directions, and scaled only in vertical direction, to align the peak positions of In-Sb 5/2, as shown in Fig. 7.4. The shifts in the horizontal direction are all smaller than 0.1 eV. The more normal way is to use Au as calibration. However, in this experiment, half of the Au peaks are poorly defined, possibly due to the small sweep number.

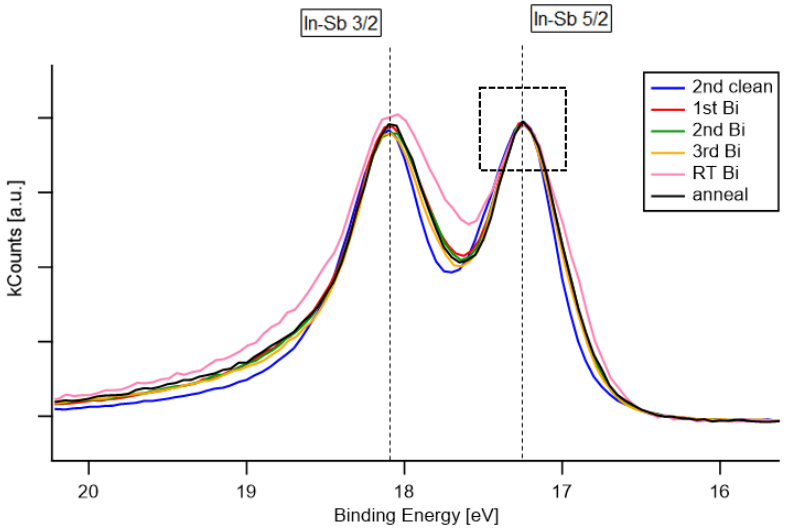

Figure 7.4: XPS spectra of In 4d core level. The dotted black frame indicates the calibration peak position. The sample here is InSb(111)A. Photon energy is 130 eV for all spectra.

In Fig. 7.4, for the spectrum of clean surface, i.e. the blue curve, the intensity ratio of the spin-orbit splitting peaks is obviously higher than the theoretical value of 0.67. And In-Sb 3/2 has a shoulder at the higher energy side. It implies there exists a non-negligible component. Recall the In-O component identified in the previous section, we deduce that there could be some oxide residue. It could also be the surface In-Sb component, which has a chemical shift compared to the bulk In-Sb.

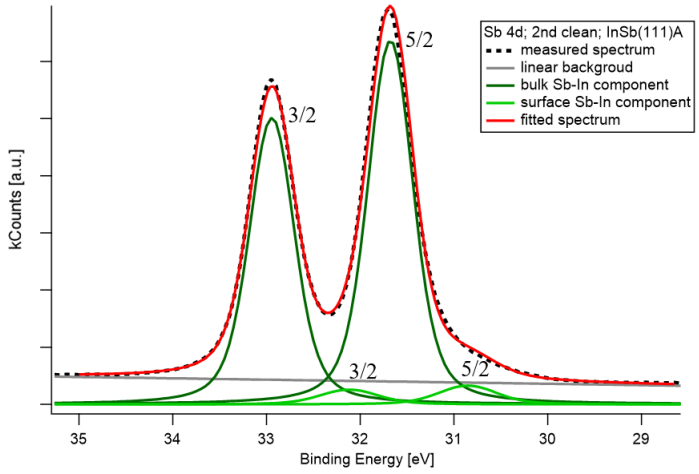

Background	Linear background
Lorentzian (eV)	0.22± 0
Ratio	1.27 ± 0
Spin-orbit splitting (eV)	1.265 ± 0
Gaussian_bulk	0.4412 ± 0.00416
Position_bulk	31.678 ± 0
Gaussian_surface	0.61447 ± 0.0781
Position_surface	30.854 ± 0.0305

Figure 7.5: XPS spectrum of Sb 4d core level on a clean InSb(111)A surface. The spectrum is fitted with two doublets components: the bulk component and the surface component.

The Bi-related surface modification induces the spectra change in Fig. 7.4. The spectra of "1st Bi" to "3rd Bi" and "anneal" are very similar to each other, but slightly different from that of clean InSb. Thus, there is a slightly different bonding configuration. This can be due to a small amount of In-Bi bonds, or just because the surface component of clean InSb is gone. While for the spectrum "RT Bi", the difference is clear. This is due to the excessive Bi layers added by the RT Bi deposition. The In atoms at the

interface in this case have a clearly different chemical environment.

When it comes to Sb, the spectrum of the clean surface exhibits a reasonable intensity ratio and a small component at the lower energy side. Peak fitting is performed, and detailed properties of the peak shape are shown in Fig. 7.5. There are two doublets including the dominant one from the InSb bulk and the small one at lower binding energy, which can be attributed with the surface. Their difference in binding energy is 0.82 eV, which is due to the surface reconstruction with different bonding configurations (as discussed in Chapter 6).

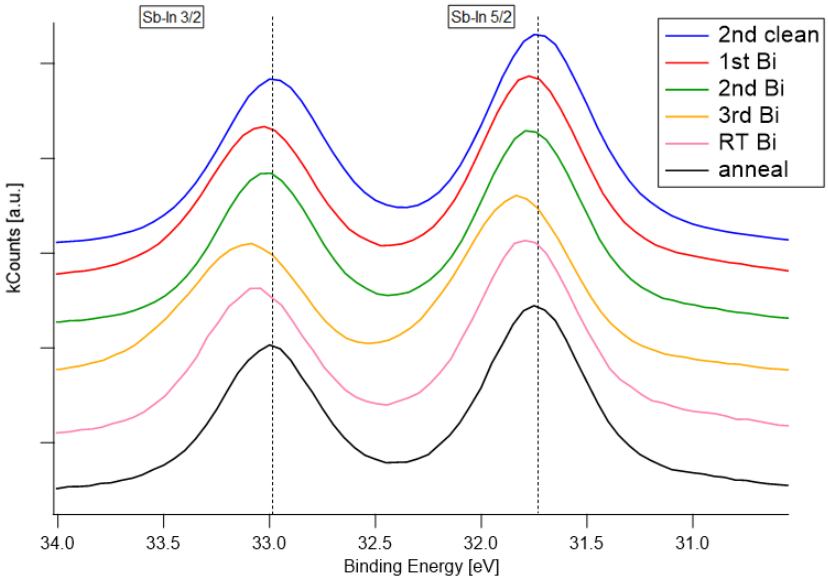

Figure 7.6: XPS spectra of Sb 4d core level. The dotted lines indicate the peak positions of the clean surface spectrum. The sample here is InSb(111)A. The InSb(111)B sample shows similar behavior. Photon energy is 130 eV for all spectra.

During surface treatments with Bi, the chemical environment of the Sb atoms is changed. As shown in Fig. 7.6, there are minor chemical shifts smaller than 0.1 eV after each procedure. The peak position keeps shifting to higher energy after each Bi deposition with the sample heated. This is due to the formation of Sb-Bi bondings, which will be clearer in the next section. With the RT Bi deposition, the added thick metallic Bi layer changes the chemical environment in another way, making the peak shift back to lower energy. The annealing process brings the spectrum back.

7.4 Spectra of Bi

The Bi 5d core level is the focus of this section.

With reliable calibrations, the relative amount of the component can be revealed by the comparison of the peak intensity in each spectrum. As shown in Fig. 7.7, the general tendency of Bi content concentration is not surprising: more Bi deposition procedures lead to higher concentration, especially for the RT Bi deposition. After annealing, the concentration falls back.

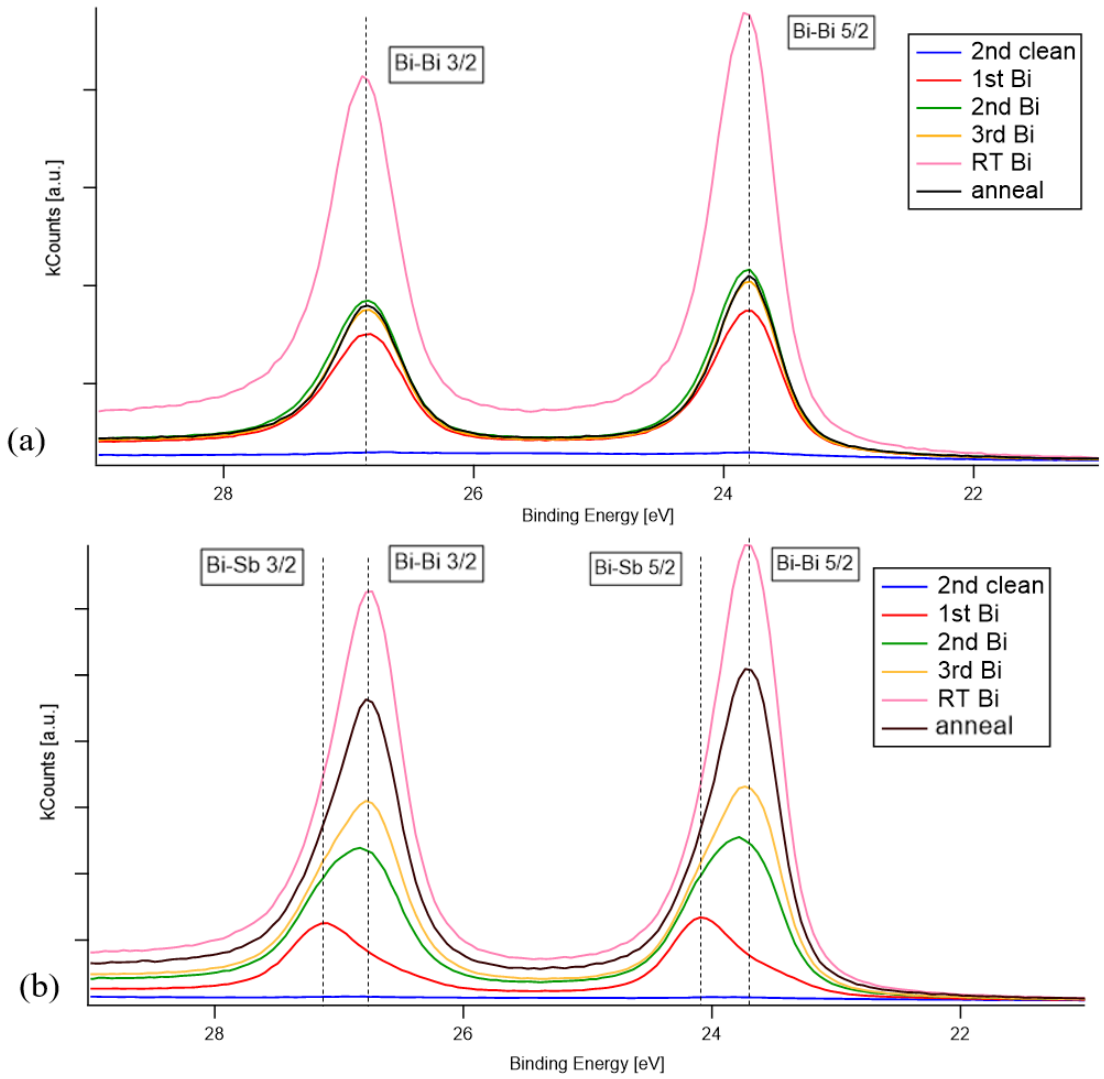

Figure 7.7: XPS spectra of Bi 5d core level. (a) The sample is InSb(111)A. (b) The sample is InSb(111)B. Photon energy is 130 eV for all spectra.

For spectra of InSb(111)A sample shown in 7.7 (a), the peak position of the doublet remains almost the same, with the Bi 5d 5/2 peak at about 23.8 eV. While for spectra of InSb(111)B sample shown in 7.7 (b), the Bi 5/2 peak initially is at about 24.1 eV and shifts gradually to 23.8 eV as the Bi concentration goes up. Apparently, the spectrum with the most Bi concentration has the most Bi-Bi component coming from the metallic Bi. Therefore 23.8 eV is identified as the binding energy of the Bi-Bi component. As mentioned before In4d remains fairly constant and with the chemical shift in Sb 4d spectra induced by Bi incorporation, we deduced that the other component at higher energy is the Bi-Sb component. Therefore the story here is the Bi atoms first bond with the Sb atoms on the surface, and with more accumulation, Bi atoms form metallic Bi.

Take the "2nd Bi" spectrum of InSb(111)B as an example. The fitted spectrum is shown in Fig. 7.8. In this case, the contributions of the Bi-Bi component and Bi-Sb component are similar in intensity. This implies that the metallic Bi layer, which is assumed to sit on top of the Bi-Sb interface layer, is still thin enough so that the

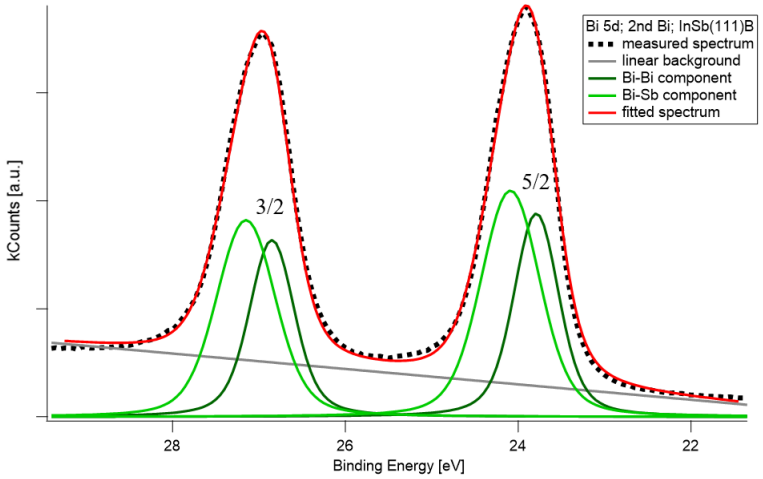

Background	Linear background
Lorentzian (eV)	0.23± 0
Ratio	1.15 ± 0
Spin-orbit splitting (eV)	3.06 ± 0
Gaussian_Bi-Bi	0.48237 ± 0
Position_Bi-Bi	23.79 ± 0
Gaussian_Bi-Sb	0.67578 ± 0
Position_Bi-Sb	24.09 ± 0

Figure 7.8: XPS spectrum of Bi 5d core level on the InSb(111)B surface which went through two Bi deposition processes. The spectrum is fitted with two doublets components: the Bi-Bi component and the Bi-Sb component.

photoelectron signal from the Bi-Sb part at the interface is not completely attenuated.

However, why the spectra of InSb(111)A show only little Bi-Sb component remains in question. We notice that the result is inconsistent with preliminary XPS measurements on a different sample. Since there is only the Bi-Bi component, this implies either too few Bi-Sb bonds are formed, or the metallic Bi accumulates too much. From the chemical shift observed in Sb 4d spectra, we tend to believe it is Bi growing too fast. One thing noticed is that previously the InSb(111)A and InSb(111)B samples on the same sample plate were not evenly cleaned by atomic hydrogen treatments. This could be due to uneven sample temperature. The InSb(111)A sample is probably not heated to the desired temperature. With a lower sample temperature, Bi accumulates faster, as Bi deposition more resembles the RT Bi deposition, and less Bi-Sb is formed. The metallic layer could already be thick enough to make the Bi-Sb component invisible. And after the second Bi deposition, the evaporation and adhesion reach equilibrium, with the sample at some temperature T higher than RT. This explains why the third regular Bi deposition does not add up more, but the RT Bi deposition still significantly increases the Bi concentration. The final annealing process at the same temperature T evaporates the excess Bi away to bring the concentration back to equilibrium. However, the discussion above is hypothetical.

8 Conclusion and Outlook

8.1 Conclusion

This thesis work experimentally investigates the surface properties of InSb(111)A/B with Bi incorporation. It exploits highly surface-sensitive characterization methods, scanning tunneling microscopy (STM) and X-ray photoelectron spectroscopy (XPS). The former is capable of mapping the surface topography at the atomic resolution, while the latter can reveal the elemental information and bonding configurations on the surface. Together they complimentarily help to understand the surface modifications happening on our samples before/after the Bi incorporation procedures.

In this study, I have reached the goal of characterizing and comparing the clean and Bi-deposited InSb surfaces. The formation of Bi layers and the bonding configurations during Bi deposition procedures are successfully understood. However, the atomic-scale structure of the deposited Bi films is not well-ordered and needs to be improved upon future studies. The influence of sample temperatures on the growth of Bi layers is also studied and well explained.

With STM, the surface reconstructions and Bi adsorption behavior are studied. The sample surface is cleaned by atomic hydrogen treatment. Different from the bulk structure, the surface structure tends to undergo rearrangement. The clean InSb(111)A surface exhibits (2×2) reconstruction and has two different species of Sb atoms, which was explained by the In-vacancy buckling model. While the clean InSb(111)B surface, on the other hand, shows (3×3) reconstruction which possesses two types of atomic structures with six-fold symmetry. This was explained as the hexamer structure model. With 15 minutes of Bi deposition, the InSb(111)A/B sample surface displays amorphous piles of Bi atom aggregations.

With XPS, the evolution of In, Sb, and Bi core-level spectra during a sequence of sample treatments is analyzed. After the oxides removal, samples are treated with Bi depositions at 250 °C and room temperature, followed by an annealing process. For clean surfaces, the surface components, which are different from the bulk component, are resolved. The chemical shifts due to the surface modification by Bi atoms are identified. Inferred from the Sb and Bi spectra, it can be concluded that there exists an Sb-Bi bonding configuration. This is an important result, as it shows that it is possible to form bonds between Bi atoms and the InSb surface, with high local Bi content. Peak fitting is performed to quantitatively analyze the components of spectra. In addition, the change of the Bi content concentration throughout the procedures is discussed.

The measurements of STM and XPS can verify and complement each other, since they share the same surface treatments. For clean surfaces, the reconstructions directly observed by STM can explain the chemical shift of the surface component from the

bulk component in XPS. On the other hand, the surface/bulk components resolved in XPS verify the different bonding configurations on the surface from that of the bulk. For surfaces with Bi deposition, the Bi atom aggregations observed by STM support the claim of Bi-Bi bonding from the metallic Bi layer in XPS. On the other hand, the Bi-Sb bonding configuration identified in XPS motivates us to discover novel structures at the InSb-Bi interface with STM.

8.2 Outlook

I have quite some regrettable things in this journey, (which will be put into the self-reflection part), and also more things that I wish that I could do specifically in the STM study. First, more Bi depositions with controlled variables like time, should be performed. With a thinner Bi layer, there is a chance to discover novel structures of Bi-Sb bonding configurations on the surface. Also, it would be interesting to explore other InSb planes like the unpolarized (110) surface and do Bi deposition on them. Besides the zinc blende structure, wurtzite InSb nanostructures are also worth trying, for example, nanoplates and nanowires. Nanowires have different facets, therefore I expect more Bi incorporation behaviors.

As the twin method of STM, scanning tunneling spectroscopy (STS) is the next technique to apply. It can reveal the DOS of the surface. Although STM and XPS together are powerful tools to reveal both the topography and bonding configurations, one key property of semiconductors is missing, which is the band structure. Angle-resolved photoemission spectroscopy (ARPES) can be introduced to future studies. It can also aid to study the surface topological properties. As a popular complementary technique, density function theory (DFT) calculations could be performed.

Bibliography

[1] Alexander T. Vogel, Johannes de Boor, Joerg V. Wittemann, Samuel L. Mensah, Peter Werner and Volker Schmidt. "Fabrication of High-Quality InSb Nanowire Arrays by Chemical Beam Epitaxy". In: *Crystal Growth & Design* 11.5 (2011), pp. 1896–1900. ISSN: 1528-7483. DOI: 10.1021/cg200066q. URL: https://doi.org/10.1021/cg200066q.

[2] S. Nadj-Perge, V. S. Pribiag, J. W. G. van den Berg, K. Zuo, S. R. Plissard, E. P. A. M. Bakkers, S. M. Frolov and L. P. Kouwenhoven. "Spectroscopy of Spin-Orbit Quantum Bits in Indium Antimonide Nanowires". In: *Phys. Rev. Lett.* 108 (16 2012), p. 166801. DOI: 10.1103/PhysRevLett.108.166801. URL: https://link.aps.org/doi/10.1103/PhysRevLett.108.166801.

[3] Jan Chochol, Kamil Postava, Michael Čada and Jaromír Pištora. "Experimental demonstration of magnetoplasmon polariton at InSb(InAs)/dielectric interface for terahertz sensor application". In: *Scientific Reports* 7.1 (2017), p. 13117. ISSN: 2045-2322. DOI: 10.1038/s41598-017-13394-0. URL: https://doi.org/10.1038/s41598-017-13394-0.

[4] S. Ahish, Dheeraj Sharma, M. H. Vasantha and Y. B. N. Kumar. "Design and Analysis of Novel InSb/Si Heterojunction Double Gate Tunnel Field Effect Transistor". In: *2016 IEEE Computer Society Annual Symposium on VLSI (ISVLSI)*. 2016, pp. 105–109. DOI: 10.1109/ISVLSI.2016.52.

[5] Zedong Yang, Brett Heischmidt, Sasa Gazibegovic, Ghada Badawy, Diana Car, Paul A. Crowell, Erik P.A.M. Bakkers and Vlad S. Pribiag. "Spin Transport in Ferromagnet-InSb Nanowire Quantum Devices". In: *Nano Letters* 20.5 (2020), pp. 3232–3239. ISSN: 1530-6984. DOI: 10.1021/acs.nanolett.9b05331. URL: https://doi.org/10.1021/acs.nanolett.9b05331.

[6] Önder Gül, Hao Zhang, Folkert K. de Vries, Jasper van Veen, Kun Zuo, Vincent Mourik, Sonia Conesa-Boj, Michał P. Nowak, David J. van Woerkom, Marina Quintero-Pérez, Maja C. Cassidy, Attila Geresdi, Sebastian Koelling, Diana Car, Sébastien R. Plissard, Erik P. A. M. Bakkers and Leo P. Kouwenhoven. "Hard Superconducting Gap in InSb Nanowires". In: *Nano Letters* 17.4 (2017), pp. 2690–2696. ISSN: 1530-6984. DOI: 10.1021/acs.nanolett.7b00540. URL: https://doi.org/10.1021/acs.nanolett.7b00540.

[7] S. Wang and P. Lu, eds. *Bismuth-Containing Alloys and Nanostructures*. Vol. 285. Springer Series in Materials Science Ser. 2019.

[8] M. P. Polak, P. Scharoch and R. Kudrawiec. "First-principles calculations of bismuth induced changes in the band structure of dilute Ga–V–Bi and In–V–Bi alloys: chemical trends versus experimental data". In: *Semiconductor Science and Technology* 30.9 (2015), p. 094001.

[9] Huaqing Huang, Jianpeng Liu and Wenhui Duan. "Nontrivial Z_2 topology in bismuth-based III-V compounds". In: *Phys. Rev. B* 90 (19 2014), p. 195105. DOI: 10.1103/PhysRevB.90.195105. URL: https://link.aps.org/doi/10.1103/PhysRevB.90.195105.

[10] I. Vurgaftman, J. R. Meyer and L. R. Ram-Mohan. "Band parameters for III–V compound semiconductors and their alloys". In: *Journal of Applied Physics* 89.11 (2001), pp. 5815–5875. DOI: 10.1063/1.1368156. eprint: https://doi.org/10.1063/1.1368156. URL: https://doi.org/10.1063/1.1368156.

[11] G. Binnig, H. Rohrer, Ch. Gerber and E. Weibel. "Surface Studies by Scanning Tunneling Microscopy". In: *Phys. Rev. Lett.* 49 (1 1982), pp. 57–61. DOI: 10.1103/PhysRevLett.49.57. URL: https://link.aps.org/doi/10.1103/PhysRevLett.49.57.

[12] J. Bardeen. "Tunnelling from a Many-Particle Point of View". In: *Phys. Rev. Lett.* 6 (2 1961), pp. 57–59. DOI: 10.1103/PhysRevLett.6.57. URL: https://link.aps.org/doi/10.1103/PhysRevLett.6.57.

[13] J. Tersoff and D. R. Hamann. "Theory of the scanning tunneling microscope". In: *Phys. Rev. B* 31 (2 1985), pp. 805–813. DOI: 10.1103/PhysRevB.31.805. URL: https://link.aps.org/doi/10.1103/PhysRevB.31.805.

[14] Anders Fahlman, Carl Nordling and Kai Siegbahn. *ESCA : atomic, molecular and solid state structure studied by means of electron spectroscopy*. eng. Uppsala : Almqvist and Wiksell, 1967. URL: http://lib.ugent.be/catalog/rug01:001343982.

[15] J. W. Niemantsverdriet. *Spectroscopy in Catalysis: An Introduction*. VCH, 2007.

[16] *Beamlines – MAX IV*. https://www.maxiv.lu.se/beamlines-accelerators/beamlines/. 2022.

[17] *FlexPES – MAX IV*. https://www.maxiv.lu.se/beamlines-accelerators/beamlines/flexpes/. 2021.

[18] J. L. Webb, J. Knutsson, M. Hjort, S. Gorji Ghalamestani, K. A. Dick, R. Timm and A. Mikkelsen. "Electrical and Surface Properties of InAs/InSb Nanowires Cleaned by Atomic Hydrogen". In: *Nano Letters* 15.8 (2015), pp. 4865–4875.

[19] Dr. Ebrl MBE-Komponenten GmbH. *Hydrogen Atomic Beam Source HABS 40-S-2113527*. Josef-Beyerle-Str. 18/1 71263 Weil der Stadt Germany, 2018.

[20] Dr. Ebrl MBE-Komponenten GmbH. *Low Temperature Effusion Cell NTEZ 40-10-22-S-2107249*. Josef-Beyerle-Str. 18/1 71263 Weil der Stadt Germany, 2018.

[21] Tetsuya Mishima and Toshiaki Osaka. "Profile imaging of the InSb111A,B-(2 × 2) surfaces". In: *Surface Science* 395.2 (1998), pp. L256–L260. ISSN: 0039-6028. DOI: https://doi.org/10.1016/S0039-6028(97)00870-4. URL: https://www.sciencedirect.com/science/article/pii/S0039602897008704.

[22] A. Proessdorf, P. Rodenbach, F. Grosse, M. Hanke, W. Braun, H. Riechert, W. Hu, S. Fujikawa, M. Kozu and M. Takahasi. "The physical origin of the InSb(111)A surface reconstruction transient". In: *Surface Science* 606.17 (2012), pp. 1458–1461. ISSN: 0039-6028. DOI: https://doi.org/10.1016/j.susc.2012.05.017. URL: https://www.sciencedirect.com/science/article/pii/S0039602812001884.

[23] Kunishige Oe, Seigo Ando and Koichi Sugiyama. "RHEED Study of InSb Films Grown by Molecular Beam Epitaxy". In: *Japanese Journal of Applied Physics* 19.7 (1980), p. L417. DOI: 10.1143/JJAP.19.L417. URL: https://dx.doi.org/10.1143/JJAP.19.L417.

[24] Masayasu Nishizawa, Toyoaki Eguchi, Tetsuya Misima, Jun Nakamura and Toshiaki Osaka. "Structure of the InSb(111)$A-(2\sqrt{3}\times 2\sqrt{3})-R30°$ surface and its dynamical formation processes". In: *Phys. Rev. B* 57 (11 1998), pp. 6317–6320. DOI: 10.1103/PhysRevB.57.6317. URL: https://link.aps.org/doi/10.1103/PhysRevB.57.6317.

[25] Masayasu Nishizawa, Toyoaki Eguchi, Sei ichi Omoto and Toshiaki Osaka. "STM study of the InSb(111)A-(2 × 6) surface". In: *Applied Surface Science* 121-122 (1997). Iketani-6, pp. 204–207. ISSN: 0169-4332. DOI: https://doi.org/10.1016/S0169-4332(97)00289-4. URL: https://www.sciencedirect.com/science/article/pii/S0169433297002894.

[26] J. Wever, H.L. Meyerheim, W. Moritz, V. Jahns, D. Wolf, H. Schulz, L. Seehofer and R.L. Johnson. "A new type of reconstruction on the InSb(1x0304;1x0304;1x0304;) surface determined by grazing incidence X-ray diffraction". In: *Surface Science* 321.3 (1994), pp. L225–L232. ISSN: 0039-6028. DOI: https://doi.org/10.1016/0039-6028(94)90179-1. URL: https://www.sciencedirect.com/science/article/pii/0039602894901791.

[27] D. Schiferl and C. S. Barrett. "The crystal structure of arsenic at 4.2, 78 and 299°K". In: *Journal of Applied Crystallography* 2.1 (1969), pp. 30–36. DOI: 10.1107/S0021889869006443. URL: https://doi.org/10.1107/S0021889869006443.

[28] Chen Liu, Yinong Zhou, Guanyong Wang, Yin Yin, Can Li, Haili Huang, Dandan Guan, Yaoyi Li, Shiyong Wang, Hao Zheng, Canhua Liu, Yong Han, James W. Evans, Feng Liu and Jinfeng Jia. "Sierpiński Structure and Electronic Topology in Bi Thin Films on InSb(111)B Surfaces". In: *Phys. Rev. Lett.* 126 (17 2021), p. 176102. DOI: 10.1103/PhysRevLett.126.176102. URL: https://link.aps.org/doi/10.1103/PhysRevLett.126.176102.

[29] *NIST X-ray Photoelectron Spectroscopy (XPS) Database, Version 3.5*. https://srdata.nist.gov/x